www.czasopisma.pan.pl PAN POLSKA AKADEMIA NAUK www.journals.pan.pl

Arch. Metall. Mater. **68** (2023), 2, 659-671

DOI: https://doi.org/10.24425/amm.2023.142447

XUE-MEI WANG[1,2], WEI ZHAO[1,2,3*], KAI CHEN[1,2], ZHEN LI[1,2]

EFFECTS OF WELDING HEAT INPUT ON MICROSTRUCTURE AND CORROSION CHARACTERIZATION IN CGHAZ OF X80 PIPELINE STEEL

The coarse-grained heat-affected zone specimens of X80 pipeline steel were produced by welding thermal simulation under different heat inputs of 10, 30, and 55 kJ/cm to study the effects of heat input on microstructure evolution and corrosion characterization. The corrosion resistance of coarse-grained heat-affected zones was poorer than that of base metal due to less homogenous in the former. For 10 kJ/cm coarse-grained heat-affected zone, the corrosion resistance was poorer than the others due to the more adsorption hydrogen around the needle-like martensite/austenite constituents and greater galvanic driving force between the needle-like martensite/austenite constituents and ferrite. In carbonate/bicarbonate solution, better corrosion resistance for coarse-grained heat-affected zones was obtained when the heat input is 30 kJ/cm, which can be attributed to the severe coarse martensite/austenite constituents for 55 kJ/cm coarse-grained heat-affected zone. In the H_2S environment, the better corrosion resistance for coarse-grained heat-affected zone was obtained when the heat input is 55 kJ/cm, which can be attributed to the protective effect of corrosion products. In addition, the high content of M/A constituents for 30 kJ/cm CGHAZ was good for hydrogen adsorption, which was adverse to the corrosion resistance in acid environments.

Keywords: X80 pipeline steel; coarse grain heat-affected zone; heat input; corrosion

1. Introduction

Pipeline transportation has been used widely for the massive exploitation of oil and natural gas [1,2]. For pipeline materials suffered corrosion in the underground environment, the properties of pipeline materials were required to be higher [3]. American Petroleum Institute (API) X80 pipeline steel, with high strength, large diameter and thin wall-thickness [4], has been used widely for long-distance transportation [5].

Corrosion of buried underground pipelines is usually induced by internal delivery products or external soil. Anti-corrosion design has become an important issue in the transportation industry [6,7]. Golchinvafa et al. [8] found that the corrosion resistance of X80 pipeline steel increases with the use of Fumaria officinalis inhibitor. Alvarez et al. [9] found that the extract of Rollinia occidentalis as well as pure solutions of two acetogenins isolated from this extract act as corrosion inhibitors for the tested C-steel in 1 M HCl media. In addition, anode control and cathode control can also improve corrosion resistance [10,11]. However, these methods of preventing corrosion are subject to environmental influences, installation conditions, and economic constraints.

The microstructure and properties of the welded joint are complicated due to the welding thermal cycles. As well known, the poor corrosion resistance of heat-affected zone (HAZ) is the main problem, restricting the use of pipeline steel [12]. Zhang et al. [13] found that the passive current density of HAZ is higher than those of weld metal and base metal (BM) in carbonate/bicarbonate solution. Wang et al. [14] found that the HAZ shows the highest charge transfer resistance and the most positive current density in the acidic soil solution. Moreover, the corrosion problems are more serious in the coarse-grained heat-affected zone (CGHAZ). Wu et al. [15] found that the CGHAZ presents the highest stress corrosion cracking (SCC) susceptibility due to coarse microstructure and high local dislocation density. Ma et al. [16] also found that the SCC susceptibility of CGHAZ is higher than that of BM due to the anodic dissolution (AD) and hydrogen embrittlement (HE) in the simulated SO_2-polluted marine atmosphere. Thus, it is necessary to study the corrosion behaviors in CGHAZs of X80 pipeline steel in deep.

[1] QILU UNIVERSITY OF TECHNOLOGY (SHANDONG ACADEMY OF SCIENCES), SCHOOL OF MECHANICAL & AUTOMOTIVE ENGINEERING, CHINA
[2] SHANDONG INSTITUTE OF MECHANICAL DESIGN AND RESEARCH, CHINA
[3] SCHOOL OF MATERIALS SCIENCE AND ENGINEERING, TIANJIN UNIVERSITY, CHINA

* Corresponding author: zwapple@yeah.net, zhaowei@qlu.edu.cn

TABLE 1

Chemical compositions of X80 pipeline steel (wt%)

C	Si	Mn	P	S	Cr	Ni	Mo	V	Cu	Al	Nb	Ti	Fe
0.046	0.30	1.76	0.0075	0.0014	0.023	0.22	0.23	0.008	0.22	0.06	0.08	0.015	Balance

Previous studies indicate that [17,18] there is a relationship between microstructure and corrosion resistance. Gennari et al. [19] found that higher volume fraction of ferrite (60%) within the joint reduces the critical pitting temperature of the weld and affects the corrosion resistance. Ashari et al. [20] found that the corrosion rate of acicular ferrite and secondary phase zones is relatively high. Huo et al. [21] found that the corrosion resistance of recrystallized grains is significantly enhanced due to finer equiaxed grains and less homogenous. Wang et al. [14] found that the microstructure of granular bainite (GB) mixed with ferrite shows better corrosion resistance. Luo et al. [22] found that high secondary phase fraction is the main reason for the high corrosion rate of 1.5Nd alloy. Jin et al. [23] found that the corrosion resistance of Mg-Zn-Ca is better due to the refined grain size. According to the earlier studies [12,24], the relationship between the microstructure evolution and corrosion resistance of X80 pipeline steel has been studied maturely. In addition, the microstructure evolution in CGHAZ depends on the cooling rate/time (i.e. welding heat input) [25].

In the present study, effects of heat input on the microstructure and corrosion resistance in the simulated CGHAZs of X80 pipeline steel were investigated. The microstructure evolution was investigated and the corrosion resistance was analyzed by electrochemical tests. The relationship among the heat inputs, microstructure evolution and corrosion resistance were established, with emphasis on the effect of changes in M/A constituents on corrosion resistance with the increase of heat input.

2. Experimental procedures

2.1. Materials and thermo-mechanical simulation

The X80 pipeline steel, used in this study, is obtained by thermo-mechanical controlled processing. The chemical compositions (wt%) are listed in TABLE 1. For low-alloyed steels, the austenite transformation temperature A_{c1} and A_{c3} can be calculated as follows [26]:

$$A_{c1}(°C) = 723 - 10.7w(Mn) - 3.9w(Ni) + \\ + 29w(Si) + 16.7w(Cr) + 290w(As) + 6.38w(W) \quad (1)$$

$$A_{c3}(°C) = 910 - 230w(Mn)^{0.5} - 15.2w(Ni) + \\ + 44.7w(Si) + 1047w(V) + 30.5w(Mo) + 13.1w(W) \quad (2)$$

where w is the mass quality of each element. It is calculated that A_{c1} and A_{c3} of the X80 pipeline steel are 713°C and 880°C, respectively.

To obtain the simulated CGHAZ samples, some 10 mm × 1 mm × 150 mm samples of the X80 pipeline steel were subjected to thermal cycles in a Gleeble 3500 simulator. The peak temperature is 1300°C and the heating rate is 160°C/s. The heat inputs are taken as 10, 30, 55 kJ/cm, respectively, and the corresponding cooling time of $\Delta t_{8/5}$ are shown in TABLE 2. The welding thermal cycle curves are shown in Fig. 1, in which A_{c1} and A_{c3} have been marked.

TABLE 2

Specific experimental parameters of welding thermo-mechanical simulation

	CGHAZ-1	CGHAZ-2	CGHAZ-3
heat input (kJ/cm)	10	30	55
cooling time $t_{8/5}$ (s)	3.3	7.3	31.4

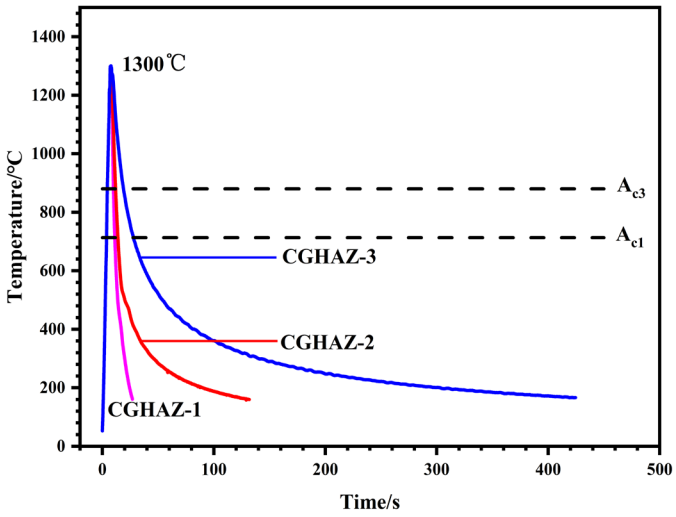

Fig. 1. Corresponding welding thermal cycle curves of simulated CGHAZs with different heat inputs

2.2. Microstructure observation and microhardness measurements

The microstructure observations of BM and simulated CGHAZ samples were performed by VHX_500F KEYENCE optical microscope (OM) after the samples were etched with 4% Nital. The martensite/austenite (M/A) constituents were identified by Le Pera solution. The composition of etchant solutions was listed in TABLE 3. Image-Pro Plus 6.0 to obtain length/width ratio, fraction and average size of the M/A constituents. The microhardness was measured by DHC-1000 type microhardness with a loading of 1.96 N and an enduring time of 15 s. Each sample was measured by 15 points randomly to calculate the average value.

TABLE 3

Composition of the etchant solutions of 4% Nital and Le pera solution

Etchant	HNO_3 (ml)	$Na_2S_2O_5$ (g)	Picric acid (g)	Water (ml)	Ethanol (ml)
4% Nital	4				96
Le pera		1	100	4	100

2.3. Immersion and Electrochemical experiments

The immersion and electrochemical experiments were conducted referring to the standard American Society for Testing Materials G3-14 and references [27-29]. The electrochemical experiments were performed using Autolab (Aut84886) with a two-component cell, Pt gauze counter electrode and saturated calomel electrode (SCE) of +0.241 V_{SHE} as a reference electrode. The electrolytes were prepared from analytical grade chemicals and distilled water. One electrolyte was a 0.5 M Na_2CO_3-1M $NaHCO_3$ solution (open to air and the pH is 9.4 at room temperature), which was mainly used to study alkaline soil corrosion of pipeline steel. The other was 5 wt% NaCl with continuous 0.1 MPa H_2S gas, which was mainly used to study H_2S corrosion inside the pipeline steel. For electrochemical measurements, all samples were polished with 100#~800# grit emery paper in turn, polished to 0.25 um with diamond paste, cleaned distilled water and alcohol in sequence, dried with cool air, and then mounted in silica gel. The area of working electrode exposed to the electrolyte was 1 cm^2. Open circuit potential (OCP) was recorded under different immersion times and the potentiodynamic polarization measurements were conducted at a scan rate of 0.5 mV/s. Electrochemical impedance spectroscopy (EIS) measurements were performed with a 10 mV amplitude and 10^5-10^{-2} Hz frequencies. In addition, the results of EIS were simulated by the ZsimDemo 3.30d.

As for alkaline soil solution, each sample was subjected to 0.5 V vs. SCE to constant potential polarization for 1 h and subjected to the Mott-Schottky curve test to study the stability of the passive film formed on the sample surfaces. The Mott-Schottky curves were obtained by a sine wave with an amplitude of 10 mV and a frequency of 1000 Hz. As for H_2S corrosion, the corrosion morphologies were observed by JSM-6480LA scanning electron microscope (SEM) with Energy dispersive X-ray spectroscopy (EDS). Corrosion products were characterized by the DX-2700 X-ray diffractometer (XRD) (Cu Ka $\lambda = 0.154060$ nm) with a scanning step of 0.02 degree/s.

3. Results

3.1. Microstructure evolution

The microstructure and microhardness of the as-received BM and simulated CGHAZs are shown in Fig. 2 and Fig. 3,

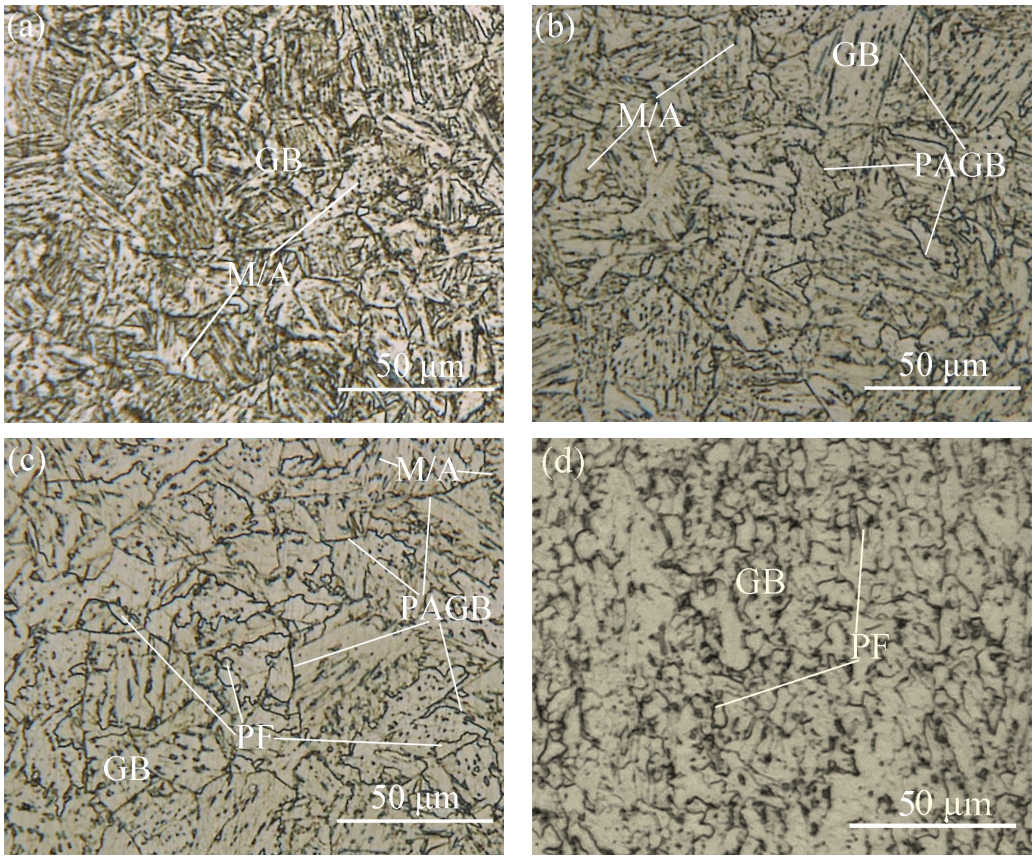

Fig. 2. Microstructure micrographs of the microstructure of CGHAZs with different heat inputs of (a) 10, (b) 30 and (c) 55 kJ/cm and (d) as-received BM

respectively. The main characteristics of the microstructure are summarized and shown in TABLE 4. The microstructure of X80 pipeline steel mainly contains polygonal ferrite (PF) and GB etched by granular M/A constituents as a secondary phase. For the BM, the M/A constituents mainly present granular with a low length/width ratio (approximately 1.46), the fraction is about 15.9% and the average size is about 0.54 μm^2. The microstructure of CGHAZ samples is mainly GB, in which the coarse prior-austenite grain boundaries (PAGB) can be seen clearly, and some PF can be seen near the PAGB only for the 55 kJ/cm. The prior-austenite grain size is all about 28 μm, indicating that it is mainly determined by the peak temperature [30]. The GB lath width increases about one time, from 0.62 μm to 1.12 μm, as the heat input increases. The M/A constituents are parallel to each other in one prior-austenite grain but not in different prior-austenite grains. For the 10 kJ/cm CGHAZ, the M/A constituents mainly present granular or needle-like with high length/width ratio (approximately 2.81). The fraction of M/A constituents is about 10.1% and the average size is about 0.64 μm^2. For the 30 and 55 kJ/cm CGHAZs, the M/A constituents mainly present granular with low length/width ratio (approximately 2.18, 1.80 respectively). Their fractions are about 14.4% and 8.2% and the average size is about 0.81 μm^2, 1.12 μm^2 respectively. The length/width ratio of the M/A constituents in CGHAZs is larger than that in BM, which decreases gradually with the increase of heat input. The fraction of M/A constituents in CGHAZs is lower than that in BM, and the highest fraction is obtained for 30 kJ/cm CGHAZ. The average size of the M/A constituents in CGHAZs is larger than that in BM, which increases gradually with the increase of heat input. In addition, the microhardness of BM is about 210 $HV_{0.2}$ and the microhardness of CGHAZs declines from about 245.78 HV to 199.36 HV as the heat input increases.

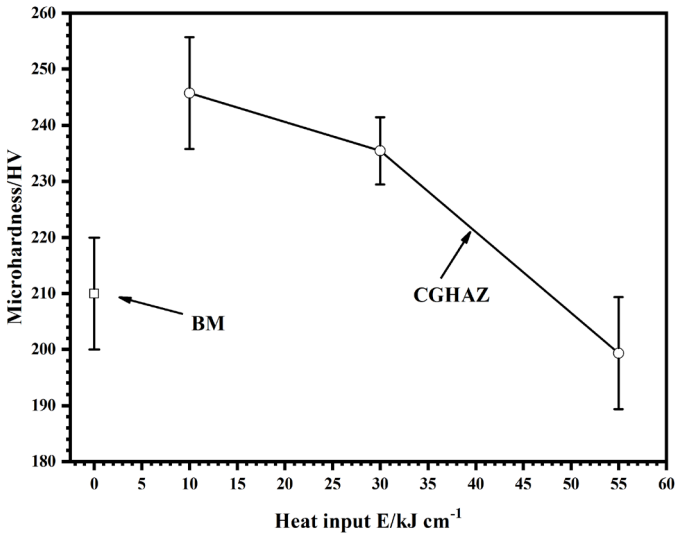

Fig. 3. Microhardness of the as-received BM and CGHAZs with different heat inputs

3.2. Corrosion characteristics in 0.5 M Na_2CO_3-1M $NaHCO_3$ environment

3.2.1. Potentiodynamic polarization curves

Fig. 4 shows the potentiodynamic polarization curves of samples in 0.5 M Na_2CO_3-1 M $NaHCO_3$ solution at room temperature, and the fitted results by extrapolation of Tafel lines are shown in TABLE 5. As shown, the shape of the potentiodynamic polarization curves and the passivation interval of as-received BM and CGHAZ samples are almost in accordance, indicating that the microstructure evolution doesn't affect the occurrence, maintenance and destruction of the passivation. When the potential attains the passivation potential E_p (about –0.70 V vs. SCE), the anodic current density begins to decrease. The current density increases firstly and decreases later with the increase of potential, which can be called a bimodal phenomenon. Later, the current density begins to keep stable with the further potential increases, which can be called "stable passivity region". When the potential rises to transpassivation potential E_{tr} (about 0.85 V vs. SCE), the current density increases with the increase of the potential. The corrosion potential E_{corr} of BM is more positive than that of CGHAZs, indicating a galvanic effect will be introduced between the BM (as a cathode) and the CGHAZ (as an anode) when the welded joint is exposed to an aggressive environment. The corrosion current density i_{corr} and passive current density i_{pass} of the BM are lower than those of the CGHAZs, indicating that corrosion resistance and the stability of the passive films are better in the former. For the CGHAZs, the E_{corr} attains the most positive, the i_{corr} and i_{pass} are the smallest when the heat input is 30 kJ/cm, indicating the corrosion resistance is better and passive film is more stable.

TABLE 4

The main microstructure characteristics of BM and CGHAZs with different heat inputs

Sample		Microstructure	Prior austenite grain size (μm)	Bainite lath size (μm)	M/A constituents			
					Shape	Length/width ratio	Fraction (%)	Average size (μm^2)
BM		PF+GB	—	—	granular	1.46	15.9	0.54
CGHAZ	10 kJ/cm	GB	27.6	0.62	needle-like/ granular	2.81	10.1	0.64
	30 kJ/cm	GB	28.1	1.06	granular	2.18	14.4	0.81
	55 kJ/cm	GB+PF	28.3	1.12	granular	1.80	8.2	1.12

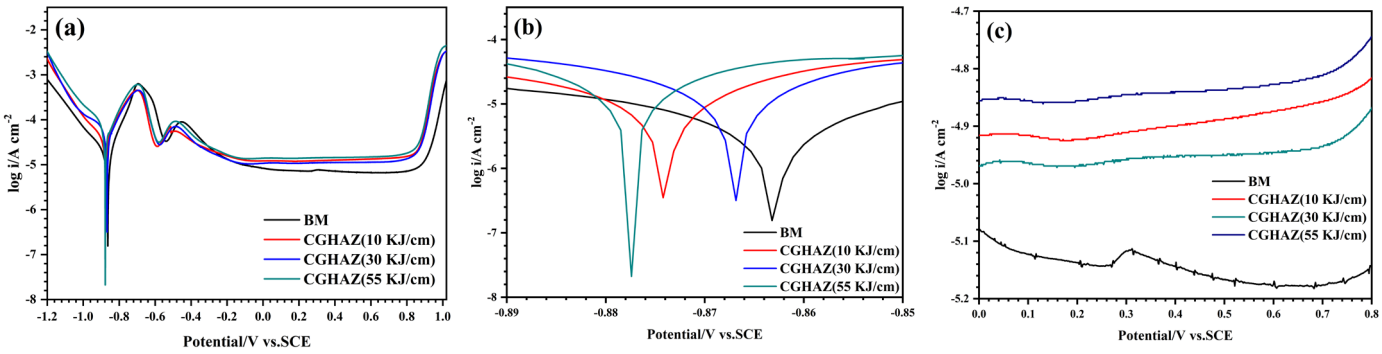

Fig. 4. Potentiodynamic polarization curves in 0.5 M Na_2CO_3-1 M $NaHCO_3$ solution: (a) The total curves, the magnification of (b) near E_{corr} and (c) stable passive region

TABLE 5

Fitted results of potentiodynamic polarization curves by extrapolation of Tafel lines

	BM	CGHAZ		
		10 kJ/cm	30 kJ/cm	55 kJ/cm
b_c (mV/dec)	208	182	300	218
E_p (V vs. SCE)	–0.453	–0.486	–0.485	–0.486
E_{tr} (V vs. SCE)	0.796	0.821	0.813	0.814
E_{corr} (V vs. SCE)	–0.843	–0.874	–0.867	–0.877
i_{corr} (μA cm^{-2})	40.28	60.32	51.36	75.34
i_{pass} (μA cm^{-2})	7.09	12.67	11.11	14.44

3.2.2. Electrochemical impedance spectroscopy

The EIS measurements of samples are conducted at OCP to study the corrosion mechanisms and the results are shown in Fig. 5. As shown, only a capacitive reactance loop exists in Nyquist impedance diagrams and one peak exists in the Bode plots, indicating only one time constant in the circuit. The impedance magnitude gradually decreases as the frequency increases and the phase angle attains the maximum value at the middle frequency. The equivalent circuit of R_s ($Q_{dl}R_{ct}$) is chosen to fit the EIS results, as shown in

Fig. 6, in which R_s is solution resistance, Q_{dl} is constant-phase element (CPE) representing the double- layer capacitance, and R_{ct} is the charge transfer resistance. The fitting results of the R_{ct}, representing the corrosion resistance, are shown in TABLE 6. The R_{ct} of the BM is larger than that of CGHAZs. For CGHAZs, the R_{ct} attains the maximum when the heat input is 30 kJ/cm. The result of EIS is in accordance with that of potentiodynamic polarization.

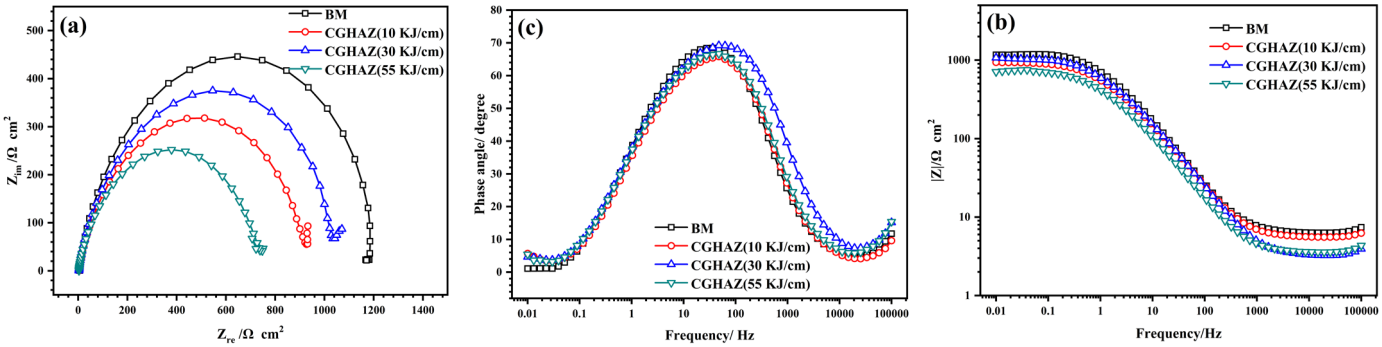

Fig. 5. EIS results of BM and CGHAZs with different heat inputs in 0.5 M Na_2CO_3-1 M $NaHCO_3$ solution: (a) Nyquist plots, Bode plots of (b) impedance magnitude vs. frequencies and (c) phase angle vs. frequencies

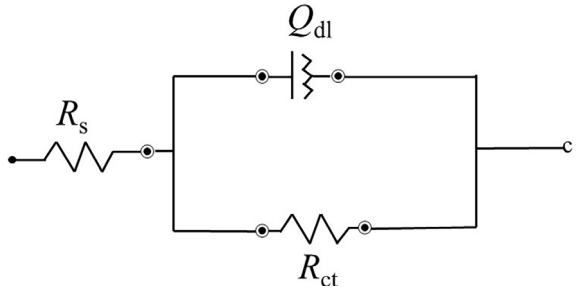

Fig. 6. Equivalent circuit of R_s ($Q_{dl}R_{ct}$)

TABLE 6

Fitted results of EIS of BM and CGHAZs with different heat inputs in 0.5 M Na_2CO_3-1 M $NaHCO_3$ solution

		BM	CGHAZ		
			10 kJ/cm	30 kJ/cm	55 kJ/cm
R_s (Ω cm^2)		6.33	5.45	5.43	3.56
Q_{dl}	Y_0 (W^{-1} cm^{-2} S^n)	181	233	218	326
	n	0.84	0.81	0.82	0.82
R_{ct} (Ω cm^2)		1188	915.6	1040	723.4

3.2.3. Mott-Schottky curves

The Mott-Schottky measurements are conducted to study the passive film characterization and the results are shown in Fig. 7. A two-slope phenomenon is observed in Mott-Schottky plots, where one linear region occurs in the potential range of −0.20 V vs. SCE to 0.20 V vs. SCE and the other occurs in the potential range of 0.30 V vs. SCE to 0.70 V vs. SCE. The shape of the Mott-Schottky curve indicates that the passive film belongs to n-type semiconductors [13,31], which the following relationships exist [13, 32-34]:

$$\frac{1}{C^2} = \frac{2}{eN_d \varepsilon \varepsilon_0 A^2}\left(E - \varphi_{fb} - \frac{kT}{e}\right) \tag{3}$$

where C is the capacitance, e is the electronic charge amount of 1.60×10^{-19} C, N_d is the average donor density of n-type, ε is the Fe_2O_3 dielectric constant of 15.6 [35], ε_0 is the vacuum dielectric constant of 8.85×10^{-14} F/cm, and A is the working electrode area of 1 cm^2, E is the test potential, φ_{fb} is the flat band potential, and k is the Boltzmann constant of 1.38×10^{-23} J/K [36], T is the absolute temperature.

The fitted results of the N_d and φ_{fb} are shown in Fig. 8. The N_d of each sample is on the order of 10^{21} cm^{-3}, indicating a highly doped semiconductor structure existed in the passive film [13]. Compared with the BM, the N_d of CGHAZs is higher, indicating that the stability of the passive film is poor. For CGHAZs, the N_d attains the minimum when the heat input is 30 kJ/cm, which is in accordance with the results of the i_{pass}. The φ_{fb} refers to the electrode potential when the semiconductor band bend is zero and its negative shift means that the electron energy level is higher and more unstable [37]. The φ_{fb} of the BM is lower than the 30 kJ/cm CGHAZ and higher than the 10, 55 kJ/cm CGHAZs, indicating its electron energy level is relatively stable. For the CGHAZs, the φ_{fb} attains the most positive when the heat input is 30 kJ/cm, which is in accordance with the results of the N_d.

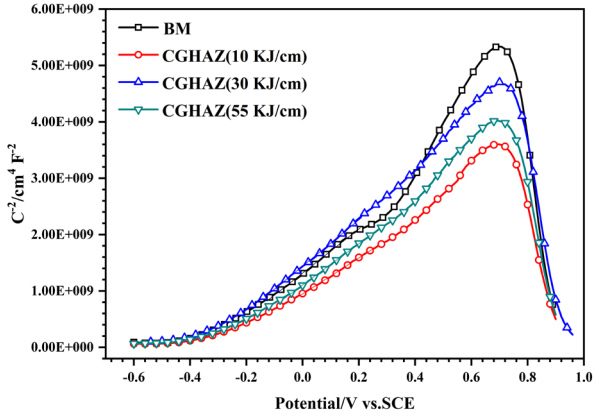

Fig. 7. Mott-Schottky curves of BM and CGHAZs with different heat inputs after potentiostatic polarization for 1 h at 0.5 V vs. SCE

3.3. Corrosion characteristics in H_2S environments

3.3.1. Open-circuit potential

Fig. 9 shows the OCP of samples under different immersion times in the H_2S environments. The OCP of all samples positively shift gradually with the development of the immersion processes, which can be attributed to the effect of the sulfide film [38]. In addition, the OCP of the CGHAZs is more negative than that of the BM within the 96 h immersion, indicating that the corrosion tendency is greater in the former. For CGHAZs, the OCP is positive shift gradually with the increase of heat input.

3.3.2. Electrochemical impedance spectroscopy

The EIS measurements are conducted at OCP and the results are shown in Fig. 10. As shown, all Nyquist impedance diagrams contain two capacitive reactance loops although the boundaries are not clear. The capacitive reactance loops in high and low frequency regions correspond to the electric double layer and corrosion process, respectively [38]. The radius size of the capacitive resistive loop for every electrode shows a similar

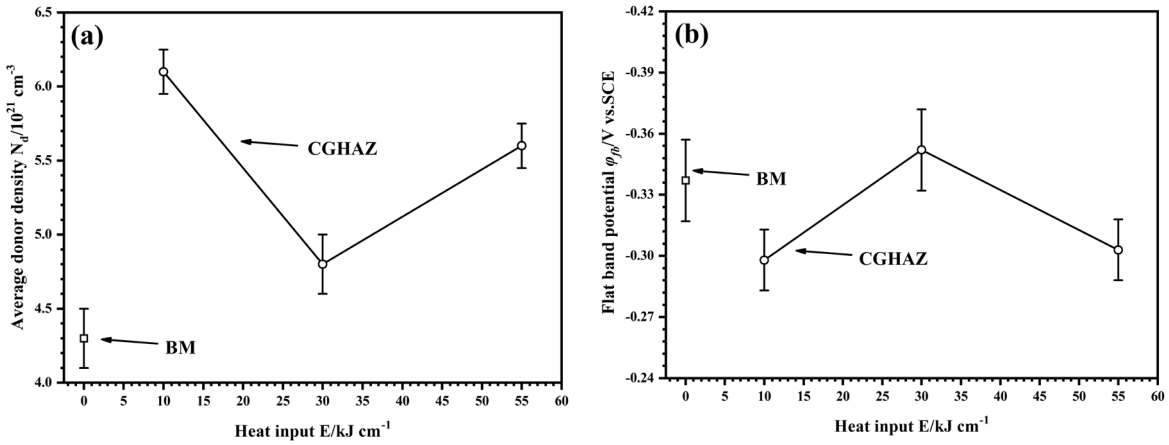

Fig. 8. The Mott-Schottky fitted results for average donor density N_d and flat band potential φ_{fb} in 0.5 M Na_2CO_3-1 M $NaHCO_3$ solution: (a) N_d and (b) φ_{fb}

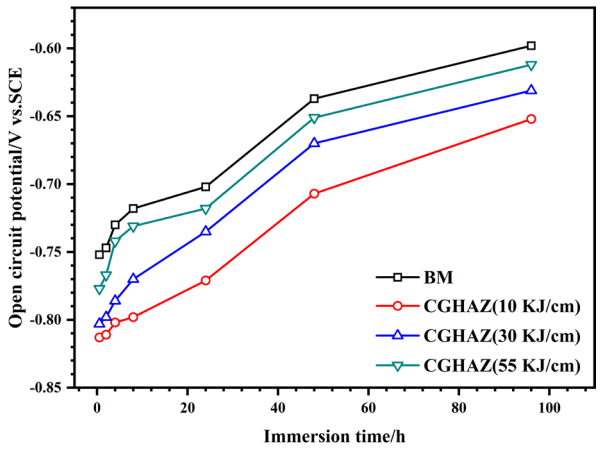

Fig. 9. OCP of BM and CGHAZs with different heat inputs in 5 wt% NaCl solution with saturated H_2S at 55°C

change with the development of the immersion processes. The equivalent circuit of R_s (Q_f (R_f ($C_{dl}R_{ct}$))) is chosen to fit the EIS results, as shown in

Fig. 11, which has been widely used in H_2S corrosion environments [12,38]. In the circuits, R_s is the solution resistance, Q_f is the CPE of corrosion products film, R_f is the resistance of the corrosion product film, C_{dl} is the double-layer capacitance and R_{ct} is the charge transfer resistance.

The fitting results of the R_f and R_{ct} are shown in Fig. 12. As shown, the R_f and R_{ct} of each electrode increase as the immersion time increases except for the mutation of immersion for 24 h. In addition, the R_f and R_{ct} of the BM are larger than those of the CGHAZs, indicating that the corrosion resistance of the BM is better. For the CGHAZs, the R_f and R_{ct} increase gradually with the increase of heat input.

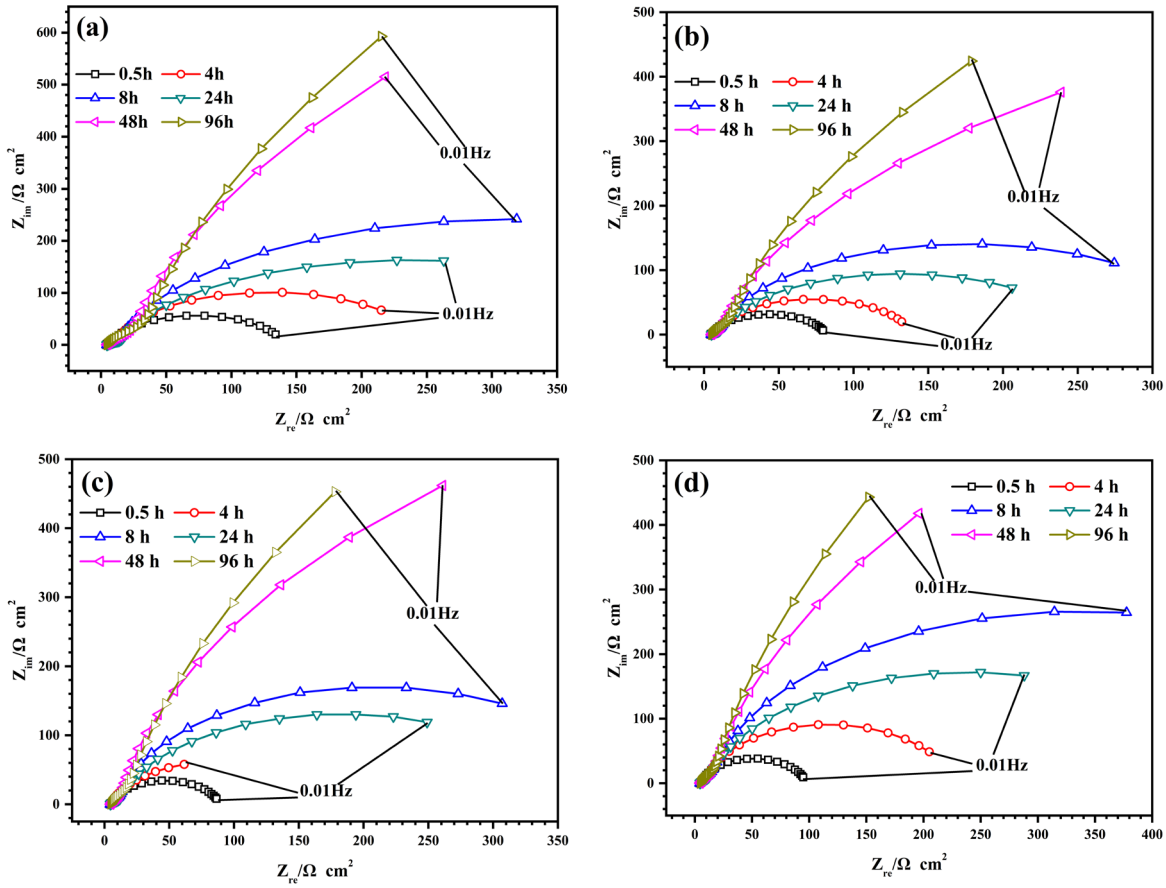

Fig. 10. Nyquist impedance diagrams of all samples in 5 wt% NaCl solution with saturated H_2S at 55°C under different immersion times: (a) BM, CGHAZs with the heat input of (b) 10, (c) 30 and (d) 55 kJ/cm

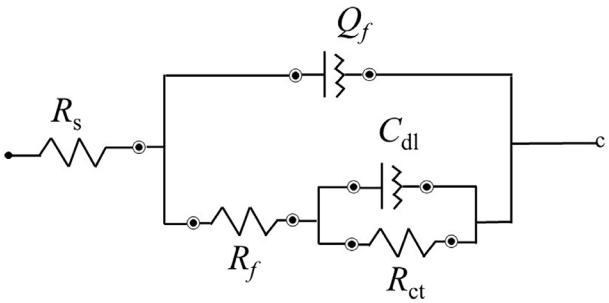

Fig. 11. Equivalent circuit of R_s (Q_f (R_f ($C_{dl}R_{ct}$)))

3.3.3. Corrosion products characterization

The SEM micrographs of corrosion product films after immersion for 96 h are shown in Fig. 13. The corresponding EDS results and XRD patterns are shown in TABLE 7 and Fig. 14. As shown, almost no difference exists in the composition of the corrosion product films for different samples. The atom ratio between Fe and S is slightly lower than 1:1 indicating that the S-enrichment corrosion products have been formed on the surface of samples after immersion for 96 h. The XRD results show that

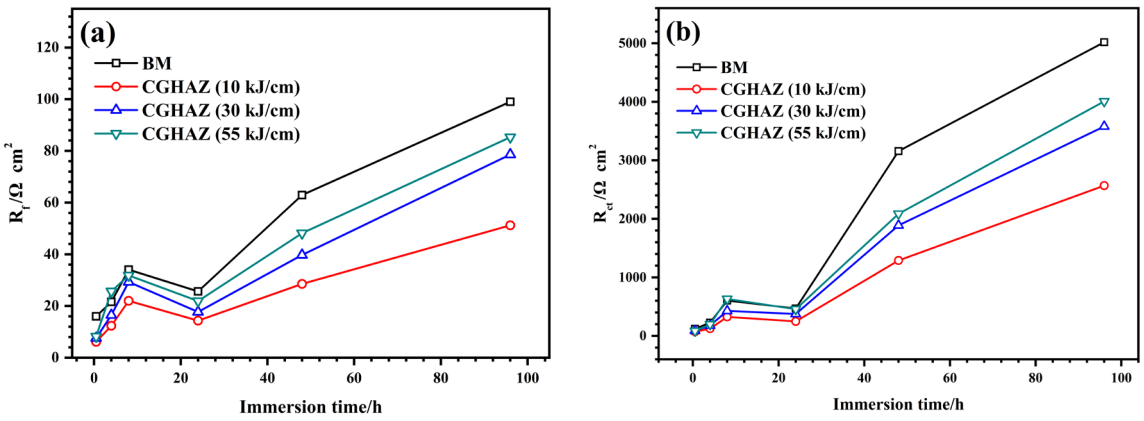

Fig. 12. Fitted results for sulfide film resistance of R_f and charge transfer resistance of R_{ct} at different immersion times: (a) R_f and (b) R_{ct}

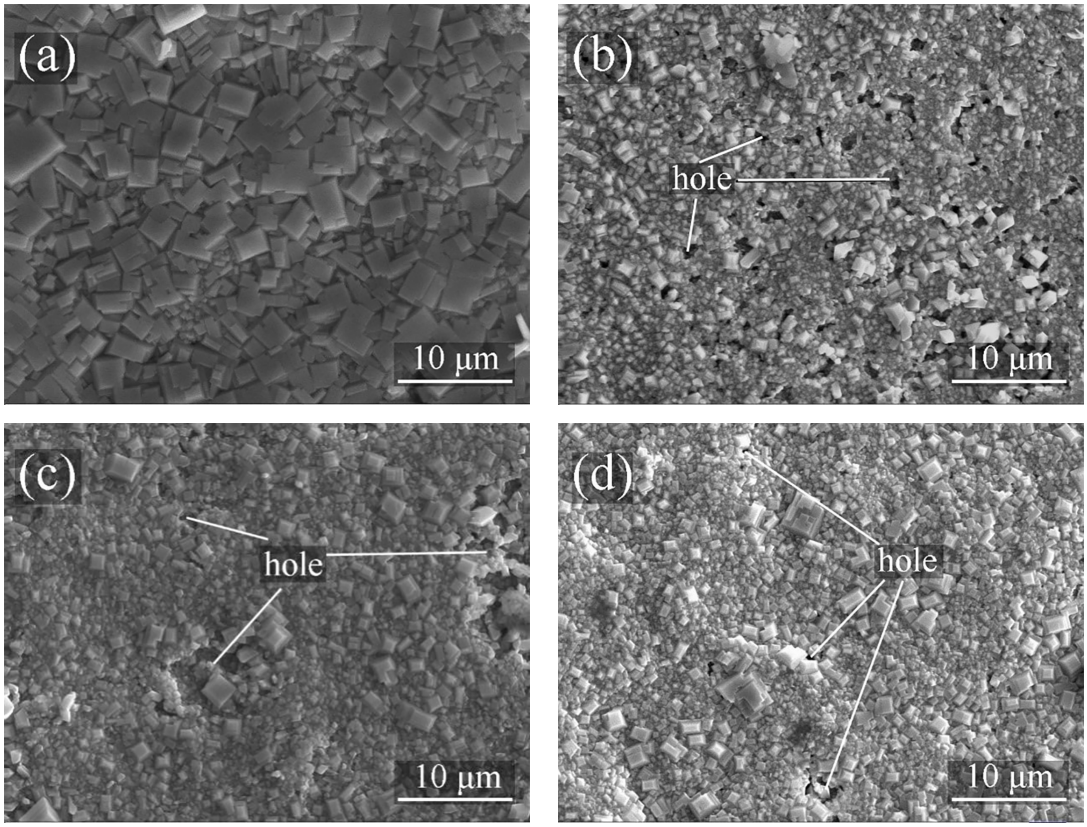

Fig. 13. SEM micrographs of corrosion products formed on all sample surfaces in 5 wt% NaCl solution with saturated H_2S at 55°C after immersion for 96 h: (a) BM and CGHAZs with the heat input of (b) 10, (c) 30 and (d) 55 kJ/cm

mackinawite is the only corrosion product. However, no holes exist in the corrosion product films of BM surface, while a large number of holes exist in CGHAZs surface. For CGHAZs, the number, size and proportion of holes decrease as the heat input increases and the protective effect of the corrosion product film on the matrix is enhanced.

TABLE 7

Corresponding EDS results of corrosion products formed on all sample surfaces in 5 wt% NaCl solution with saturated H_2S at 55°C after immersion for 96 h

	BM	CGHAZ		
		10 kJ/cm	30 kJ/cm	55 kJ/cm
Fe (at.%)	44.82	43.83	45.27	46.21
S (at.%)	55.18	56.17	54.73	53.79
ratio (at.% / at.%)	1:1.23	1:1.28	1:1.21	1:1.16

4. Discussion

4.1. Electrochemical corrosion behavior in carbonate/bicarbonate solution

In carbonate/bicarbonate solution, the possible cathodic electrochemical reactions are as follows [39-41]:

$$O_2 + 2H_2O + 4e \rightarrow 4OH^- \quad (4)$$

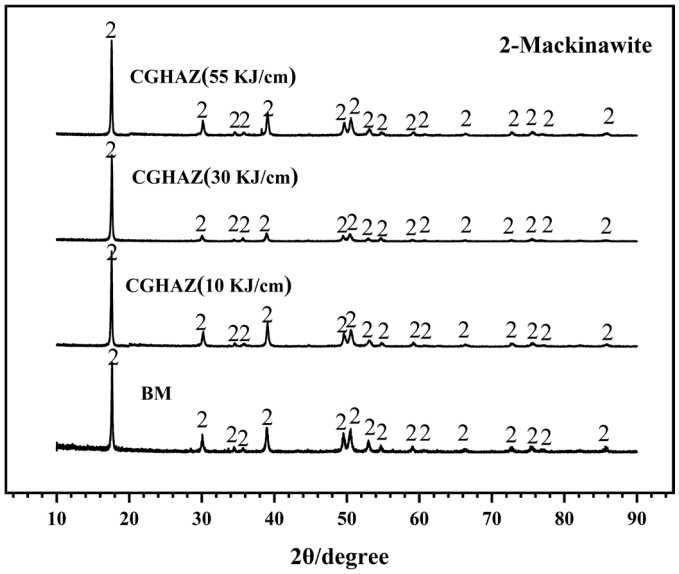

Fig. 14. Corresponding XRD patterns of corrosion products formed on all sample surfaces in 5 wt% NaCl solution with saturated H_2S at 55°C after immersion for 96 h

$$HCO_3^- + e \rightarrow CO_3^{2-} + \frac{1}{2}H_2 \quad (5)$$

$$H_2O + e \rightarrow H + OH^- \quad (6)$$

The anodic reactions are the dissolution reaction of Fe firstly, as follows [42]:

$$Fe \rightarrow Fe^{2+} + 2e \quad (7)$$

The passive phenomenon occurs due to the presence of corrosion products, such as $FeCO_3$ and $Fe(OH)_2$ [13,43], as follows:

$$Fe + HCO_3^- \rightarrow FeCO_3 + H^+ + 2e \quad (8)$$

$$Fe + CO_3^{2-} \rightarrow FeCO_3 + 2e \quad (9)$$

$$Fe + 2OH^- \rightarrow Fe(OH)_2 + 2e \quad (10)$$

The current begins to increase again when the potential increases to around –0.55V vs. SCE, which may be due to the dissolution of $Fe(OH)_2$ by OH^- [39], as follows:

$$2Fe(OH)_2 + 2OH^- \rightarrow Fe_2O_3 + 3H_2O + 2e \quad (11)$$

Moreover, the current drops again can be attributed to the dissolution of $FeCO_3$ [13,43]:

$$3FeCO_3 + 4H_2O \rightarrow Fe_3O_4 + 3HCO_3^- + 5H + 2e \quad (12)$$

$$2FeCO_3 + 3H_2O \rightarrow \gamma - Fe_2O_3 + 2HCO_3^- + 4H^+ + 2e \quad (13)$$

The stable passive region provides the possibility of anodic protection as the potential increases to about 0 V vs. SCE. In a stable passivity region, Fe can be oxidized to Fe_3O_4 directly, which can be further oxidized to Fe_2O_3, as follows [44]:

$$3Fe + 4H_2O \rightarrow Fe_3O_4 + 8H^+ + 8e \quad (14)$$

$$2Fe_3O_4 + H_2O \rightarrow Fe_2O_3 + 2H^+ + 2e \quad (15)$$

$$2Fe_3O_4 + H_2O \rightarrow 3Fe_2O_3 + 2H^+ + 2e \quad (16)$$

$$2Fe_3O_4 + H_2O \rightarrow 3\gamma - Fe_2O_3 + 2H^+ + 2e \quad (17)$$

In the transpassivation region, the electrode reaction of O_2 precipitation will also occur in addition to the continuous formation of Fe^{3+} by Fe.

The actual equilibrium electrode potential of the above anodic reactions can be calculated according to the Nernst equation, as follows [45]:

$$E_e = E_e^0 + \frac{RT}{nF}\ln\left(\prod_j a_j^{v_j}\right) \quad (18)$$

where E_e and $E0$ eare the actual and standard equilibrium electrode potentials, respectively, a and j are the activity and stoichiometric number of reactants or products, respectively. Thus, the E_e at 25°C of some anodic reactions is calculated and shown in Table 8

The Mott-Schottky plots (Fig. 6) indicate that two slopes exist in the linear range, which may be due to the nonuniform distribution of donors in the passive film, the variation of Helmholtz layer potential caused by the surface states, and the existence of two donor levels in the band gap [13]. The increase of slope at the slope-transition potential means the decrease of N_d in passive film because the N_d is inversely proportional to the slope [46]. It has been shown [47] that the main donors for an n-type semiconductor passive film are the oxygen vacancies. The decrease in the oxygen vacancy concentration at the slope-transition potential is attributed to the Fe^{2+} in Fe_3O_4 being oxidized to Fe^{3+} by absorbing one unit of oxygen from water. Therefore, with the further increase of passive potential, the stability of passive film will be enhanced.

4.2. Electrochemical corrosion behavior in H_2S environment

The sulfide corrosion products form and grow quickly on the steel surface because of the fast and drastic reactions between Fe and H_2S at the initial immersion stage. The ionized HS^- in H_2S adsorbs on the steel surface and forms the adsorbed ion ($FeHS^-$). The reactions are as follows [38,48]:

TABLE 8

Equilibrium electrode potentials E_e of anodic reactions (V vs. SCE)

Equation	8	9	10	11	12	13	14	15	16	17
E_e	–1.28	–0.99	–0.85	–0.83	–0.98	–0.73	–0.459	–0.219	–0.83	–0.23

Anodic reaction:

$$Fe + H_2S \rightarrow Fe + HS^-_{(ads)} + H^+_{(ads)} \quad (19)$$

$$Fe + HS^-_{(ads)} + H^+_{(ads)} \rightarrow FeHS^-_{(ads)} + H^+_{(ads)} \quad (20)$$

$$FeHS^-_{(ads)} + H^+_{(ads)} \rightarrow FeHS^+_{(ads)} + H_{(ads)} + e \quad (21)$$

Cathodic reaction:

$$FeHS^+_{(ads)} + H_{(ads)} + e \rightarrow FeS_{(ads)} + 2H_{ads} \quad 22)$$

Overall reaction:

$$Fe + H_2S \rightarrow FeS_{(ads)} + 2H_{ads} \quad (23)$$

The H_{ads} refers to the adsorption hydrogen on the electrode surface, which can combine with hydrogen molecules (H_2), or penetrate the electrode to absorption hydrogen (H_{abs}) as the concentration of H_{ads} increases. As demonstrated [49,50], the HE, hydrogen-induced crack and sulfide stress corrosion cracking can be induced by the permeation of H_{abs} in H_2S environments.

According to the atomic ratio of Fe to S, the iron sulfide can be divided into FeS, FeS_2 and intermediate transition state. The FeS mainly consists of mackinawite, cubic FeS and troilite, the FeS_2 mainly consist of pyrite and marcasite and the intermediate transition state consists of pyrrhotite, smythite and greigite [51]. Studies have found that in the anaerobic H_2S environment, the formation order of sulfide corrosion products is mackinawite, cubic FeS, troilite, pyrrhotite, pyrite [52]. Mackinawite is the only corrosion product in this study, which is formed on the steel surface by fast solid-state reaction and precipitation. As the corrosion process develops, the accumulation of the mackinawite leads to an increase in R_f. The charge transfer becomes difficult because of the inhibition effect of the sulfide film.

The corrosion products on the surface of BM samples are tightly arranged, which has a better protective effect by impeding the ion exchange. For CGHAZs, the formation of holes on the surface of corrosion products may be attributed to the fact that the microstructure is not conducive to the accumulation of corrosion products. The lattice of sulfide corrosion products formed on CGHAZ surfaces is more complete and its crystal structure is more compact at the higher heat input, which can effectively prevent the passage of cations and improve the corrosion resistance [48]. In addition, the E_{corr} of the hole zone is different from that of the surrounding area, which can easily cause pitting corrosion. It is worth noting that these holes are likely to become crack sources, leading to failure under external forces.

4.3. Effect of microstructure evolution on corrosion resistance

4.3.1. The M/A constituent evolution

The M/A constituents belong to the intermediate temperature transformation products. Firstly, ferrite is first precipitated at a relatively high temperature during the austenite cooling process. The untransformed austenite region is rich in carbon due to the formation of ferrite and the carbon-rich undercooled austenite transforms partially into martensite. Finally, the mixture of martensite and retained austenite is called the M/A constituents [25]. M/A constituents, as the secondary phase, are present in the as-received BM and the CGHAZs. However, the shape, fraction and average size of various samples are different. Compared with BM, the M/A constituents in the CGHAZs present needle-like or granular, with less quantity and large size, which is mainly due to the increase of cooling time by the effect of welding thermal cycling in the latter. Hence the cooling rate decreases, resulting in the transformation shift to higher temperature.

For 10 kJ/cm CGHAZ, the M/A constituents present needle-like, different from other specimens, and the content is relatively low which can be attributed to the insufficient carbon atom diffusion. For 55 kJ/cm CGHAZ, the M/A constituents are severely coarsened and their size becomes larger due to the slow cooling rate. In addition, ferrite exists in the microstructure mainly because ferrite nucleation becomes easier and restrains the production of M/A constituents with the increase of welding heat input and the decrease of cooling rate. Thus, the content of M/A constituents is the most for CGHAZs when the heat input is 30 kJ/cm.

4.3.2. Effect of the M/A constituents on the corrosion resistance

For the BM, the relatively fine grain, uniform distribution of the microstructure, and presence of a large sum of PF with low dislocations contributed to better corrosion resistance. In addition, the M/A constituents in the BM present granular and low length/width ratio, which leads to the galvanic effect between M/A constituents and matrix negligible [17,53]. The poor corrosion resistance of the CGHAZs is due to relatively coarse microstructure and M/A constituents. Moreover, the non-equilibrium GB, high welding residual stress, lattice distortion and dislocations are in favor of the low corrosion resistance in the CGHAZs.

For 10 kJ/cm CGHAZ, due to the large contact area between the needle-like M/A constituents and the matrix, a relatively large galvanic driving force is introduced. In addition, high potential to be hydrogen traps exists in the needle-like M/A constituents [54,55]. Thus, the corrosion resistance is poor for 10 kJ/cm CGHAZ. It is worth noting that the needle-like M/A constituents are easily to be the potential sites for crack initiation due to high stress accumulation at M/A-matrix interfaces [25]. Thus, the heat input should not be too low in practical application.

In the 0.5 M Na_2CO_3-1 M $NaHCO_3$ environment, the severe coarsening and large size of M/A constituents lead to poor corrosion resistance for 55 kJ/cm CGHAZ. Thus, the best corrosion resistance for CGHAZs is obtained when the heat input is 30 kJ/cm.

In the H_2S environment, the larger proportion of hydrogen generated by the cathodic hydrogen evolution remains in the atomic state and penetrates the matrix due to the “poisonous”

effect of H_2S and HS^- [56,57]. Wang et al. [58] found that the gap between martensite and retained austenite is the main hydrogen capture site. For 30 kJ/cm CGHAZ, the corrosion resistance is poor due to a large amount of adsorption hydrogen around M/A constituents. Thus, the best corrosion resistance for CGHAZs is obtained when the heat input is 55 kJ/cm.

5. Conclusions

(1) For CGHAZs in X80 pipeline steel, the microstructure was mainly GB embellished by M/A constituents. The lath width of GB increased with the increase of heat input. For M/A constituents, the length/width ratio decreased with the increase of heat input, while the average size increased. The content of the M/A constituents was the highest when the heat input was 30 kJ/cm.

(2) Electrochemical results showed that the corrosion resistance of BM was better than CGHAZs in the 0.5 M Na_2CO_3-1 M $NaHCO_3$ solution and H_2S environment. It can be attributed to the relatively fine grain, uniform distribution of the microstructure, and presence of a large sum of PF with low dislocations in the BM.

(3) For 10 kJ/cm CGHAZ, the corrosion resistance was poor due to the large galvanic driving force between the needle-like M/A constituents and matrix and the high hydrogen trap potential in the needle-like M/A constituents.

(4) In the 0.5 M Na_2CO_3-1M $NaHCO_3$ solution, for 55 kJ/cm CGHAZ, the corrosion resistance was poor due to the severe coarsening and large size of M/A constituents. Thus, the corrosion resistance of CGHAZs was the best when the heat input was 30 kJ/cm.

(5) In an H_2S environment, for 30 kJ/cm CGHAZ, the corrosion resistance was poor due to a large amount of adsorption hydrogen around M/A constituents. In addition, for 55 kJ/cm CGHAZ, the protective effect of the sulfide corrosion products on the matrix was enhanced. Thus, the corrosion resistance of CGHAZs was the best when the heat input was 55 kJ/cm.

Acknowledgments

The work was supported by the National Nature Science Foundation of China (No. 51805285), the Project funded by China Postdoctoral Science Foundation (2019M661016), the Key Research and Development Project of Shandong Province (2021LYXZ14), the Innovation Team Project of Jinan (2019GXRC035).

REFERENCES

[1] H.R. Vanaei, A. Eslami, A. Egbewande, A review on pipeline corrosion, in-line inspection (ILI), and corrosion growth rate models, Int. J. Pres. Ves. Pip. **149**, (2017).

[2] P.C. Okonkwo, M.H. Sliem, R.A. Shakoor, A.M.A. Mohamed, A.M. Abdullah, Effect of temperature on the corrosion behavior of API X120 pipeline steel in H_2S environment, J. Mater. Eng. Perform. **26**, (2017).

[3] S.K. Sharma, S. Maheshwari, A review on welding of high strength oil and gas pipeline steels, J. Nat. Gas Sci. Eng. **38**, (2017).

[4] X.D. Cheng, C. Ma, R.K. Huang, S.N. Huang, W.D. Yang. Failure mode analysis of X80 buried steel pipeline under oblique-reverse fault, Soil Dyn. Earthq. Eng. **125**, 105723 (2019).

[5] B. Liu, Z. Li, X. Yang, C. Du, X. Li, Microbiologically influenced corrosion of X80 pipeline steel by nitrate reducing bacteria in artificial Beijing soil, Bioelectrochemistry **135**, (2020). DOI: https://doi.org/10.1016/j.bioelechem.2020.107551

[6] B. Zhu, N. Jiang, C. Zhou, X. Luo, Y. Yao, T. Wu, Dynamic failure behavior of buried cast iron gas pipeline with local external corrosion subjected to blasting vibration, J. Nat. Gas Sci. Eng. **88**, 103803 (2021). DOI: https://doi.org/10.1016/j.jngse.2021.103803

[7] S. Kanwal, N.Z. Ali, R. Hussain, F.U. Shah, Z. Akhter, Polythiourea formaldehyde based anticorrosion marine coatings on type 304 stainless steel, J. Mater. Res. Technol. **9**, 2146 (2020). DOI: https://doi.org/10.1016/j.jmrt.2019.12.045

[8] A. Golchinvafa, S.H. Mousavi Anijdan, M. Sabzi, M. Sadeghi, The effect of natural inhibitor concentration of Fumaria officinalis and temperature on corrosion protection mechanism in API X80 pipeline steel in 1 M H_2SO_4 solution, Int. J. Pres. Ves. Pip. **188**, 104241 (2020). DOI: https://doi.org/10.1016/j.ijpvp.2020.104241

[9] P.E. Alvarez, M.V. Fiori-Bimbi, A. Neske, S.A. Brandán, C.A. Gervasi, Rollinia occidentalis extract as green corrosion inhibitor for carbon steel in HCl solution, J. Ind. Eng. Chem. **58**, 92 (2018). DOI: https://doi.org/10.1016/j.jiec.2017.09.012

[10] J.M. Jinjie Shi, Danqian Wang, Miao Wu, Improved corrosion resistance of a new 6% Cr steel in simulated concrete pore solution contaminated by chlorides, Corros. Sci. **174**, (2020).

[11] P. Dohare, K.R. Ansari, M.A. Quraishi, I.B. Obot, Pyranpyrazole derivatives as novel corrosion inhibitors for mild steel useful for industrial pickling process: Experimental and Quantum Chemical study, J. Ind. Eng. Chem. **52**, 197 (2017). DOI: https://doi.org/10.1016/j.jiec.2017.03.044

[12] W. Zhao, Y. Zou, K. Matsuda, Z. Zou, Characterization of the effect of hydrogen sulfide on the corrosion of X80 pipeline steel in saline solution, Corros. Sci. **102**, (2016). DOI: http://dx.doi.org/10.1016/j.corsci.2015.10.038

[13] G.A. Zhang, Y.F. Cheng, Micro-electrochemical characterization and Mott-Schottky analysis of corrosion of welded X70 pipeline steel in carbonate/bicarbonate solution, Electrochim. Acta **55**, 316 (2009). DOI: https://doi.org/10.1016/j.electacta.2009.09.001

[14] J. Wang, Q. Li, M.M. Li, T.H. Chen, Y.F. Zhou, Z.B. Yue, Competitive adsorption of heavy metal by extracellular polymeric substances (EPS) extracted from sulfate reducing bacteria, Bioresour. Technol. **163**, (2014). DOI: https://doi.org/10.1016/j.biortech.2014.04.073

[15] Z.L. W. Wu, X.G. Li, C.W. Du, Z.Y. Cui, Influence of different heat-affected zone microstructures on the stress corrosion behavior and mechanism of high-strength low-alloy steel in a sulfurated marine atmosphere, Mater. Sci. Eng.: A. **759**, (2019).

[16] H. Ma, Z. Liu, C. Du, X. Li, Z. Cui, Comparative study of the SCC behavior of E690 steel and simulated HAZ microstructures in a SO2-polluted marine atmosphere, Mater. Sci. Eng: A. **650**, 93 (2016).
DOI: https://doi.org/10.1016/j.msea.2015.09.052

[17] Z.P. Zhao, K. Xu, P.F. Xu, B. Wang, CO_2 corrosion behavior of simulated heat-affected zones for X80 pipeline steel, Mater Charact. **171**, 110772 (2021).
DOI: https://doi.org/10.1016/j.matchar.2020.110772

[18] Y. Zhu, Y. Xu, M. Wang, X. Wang, G. Liu, Y. Huang, Understanding the influences of temperature and microstructure on localized corrosion of subsea pipeline weldment using an integrated multi-electrode array, Ocean Eng. **189**, 106351 (2019).
DOI: https://doi.org/10.1016/j.oceaneng.2019.106351

[19] C. Gennari, M. Lago, B. Bögre, I. Meszaros, I. Calliari, L. Pezzato, Microstructural and Corrosion Properties of Cold Rolled Laser Welded UNS S32750 Duplex Stainless Steel, Metals **8**, 1074 (2018). DOI: https://doi.org/10.3390/met8121074

[20] R. Ashari, A. Eslami, M. Shamanian, S. Asghari, Effect of weld heat input on corrosion of dissimilar welded pipeline steels under simulated coating disbondment protected by cathodic protection, J. Mater. Res. Technol. **9**, 2136 (2020).
DOI: https://doi.org/10.1016/j.jmrt.2019.12.044

[21] T.T. Sun, W.T. Huo, L. G. Hou, W. Zhang, Y.S. Zhang, J.S. Zhang, Effect of heating rate during solution treatment on microstructure, mechanical property and corrosion resistance of high-strength AA 7075 alloy, Mater. Charact. **167**, (2020).

[22] Luo Y, Deng Y, Guan L, et al., The microstructure and corrosion resistance of as-extruded Mg-6Gd-2Y- (0–1.5) Nd-0.2Zr alloys. Mater Design. 2020;186.

[23] Y. Luo, Y. Deng, L. Guan, L. Ye, X. Guo, The microstructure and corrosion resistance of as-extruded Mg-6Gd-2Y- (0-1.5) Nd-0.2Zr alloys, Mater. Design. **186**, 108289 (2020).
DOI: https://doi.org/10.1016/j.matdes.2019.108289

[24] F.M. AlAbbas, C. Williamson, S.M. Bhola, J.R. Spear, D.L. Olson, B. Mishra, A.E. Kakpovbia, Influence of sulfate reducing bacterial biofilm on corrosion behavior of low-alloy, high-strength steel (API-5L X80), Int. Biodeter. Biodegr. **78**, (2013).
DOI: http://dx.doi.org/10.1016/j.ibiod.2012.10.014

[25] P. Zhou, B. Wang, L. Wang, Y. Hu, L. Zhou, Effect of welding heat input on grain boundary evolution and toughness properties in CGHAZ of X90 pipeline steel, Mater. Sci. Eng: A. **722**, 112 (2018). DOI: https://doi.org/10.1016/j.msea.2018.03.029

[26] L.W. Wang, Z.Y. Liu, Z.Y. Cui, C.W. Du, X.H. Wang, X.G. Li, In situ corrosion characterization of simulated weld heat affected zone on API X80 pipeline steel, Corros. Sci. **85**, 401 (2014).
DOI: https://doi.org/10.1016/j.corsci.2014.04.053

[27] N.R. Honesty, A.A. Gewirth, Investigating the effect of aging on transpassive behavior of Ni-based alloys in sulfuric acid with shell-isolated nanoparticle enhanced Raman spectroscopy (SHINERS), Corros. Sci. **67**, 67 (2013).
DOI: https://doi.org/10.1016/j.corsci.2012.10.002

[28] M.A. Khan, Electrochemical polarisation studies on plasma-sprayed nickel-based superalloy, Applied Physics A. **120**, 801 (2015). DOI: https://doi.org/10.1007/s00339-015-9291-0

[29] J. Xu, X. Wu, E.H. Han, Acoustic emission during the electrochemical corrosion of 304 stainless steel in H_2SO_4 solutions, Corros. Sci. **53**, 448 (2011).
DOI: https://doi.org/10.1016/j.corsci.2010.09.056

[30] F. Mohammadi, F.F. Eliyan, A. Alfantazi, Corrosion of simulated weld HAZ of API X-80 pipeline steel, Corros. Sci. **63**, 323 (2012).
DOI: https://doi.org/10.1016/j.corsci.2012.06.014

[31] I.M. Gadala, A. Alfantazi, A study of X100 pipeline steel passivation in mildly alkaline bicarbonate solutions using electrochemical impedance spectroscopy under potentiodynamic conditions and Mott-Schottky, Appl. Surf. Sci. **357**, 356 (2015).
DOI: https://doi.org/10.1016/j.apsusc.2015.09.029

[32] D.G. Li, Y.R. Feng, Z.Q. Bai, J.W. Zhu, M.S. Zheng, Photoelectrochemical analysis of passive film formed on X80 pipeline steel in bicarbonate/carbonate buffer solution, Appl. Surf. Sci. **254**, 2837 (2008).
DOI: https://doi.org/10.1016/j.apsusc.2007.10.036

[33] A.Q. Fu, Y.F. Cheng, Electrochemical polarization behavior of X70 steel in thin carbonate/bicarbonate solution layers trapped under a disbonded coating and its implication on pipeline SCC, Corros. Sci. **52**, 2511 (2010).
DOI: https://doi.org/10.1016/j.corsci.2010.03.019

[34] Y.R. Feng. D.G. Li, Z.Q. Bai, J.W. Zhu, M.S. Zheng, Influence of temperature chloride ions and chromium element on the electronic property of passive film formed on carbon steel in bicarbonate carbonate buffer solution, Electrochim. Acta **52** (28), 7877-7884 (2007).
DOI: https://doi.org/10.1016/j.electacta.2007.06.059

[35] X.G. Li, L. Zhang, C.W. Du, Effect of environmental factors on electrochemical behavior of X70 pipeline steel in simulated soil solution, J. Iron Steel Res. Int. **16**, 52-57, (2009).

[36] L. Pitre, M.D. Plimmer, F. Sparasci, M.E. Himbert, Determinations of the Boltzmann constant, CR Phys. **20**, 129 (2019).
DOI: https://doi.org/10.1016/j.crhy.2018.11.007

[37] C. Zhang, J.H. Zeng, Y.F. Wang, Manganese doped titanium dioxide with a tunable flat-band potential as photoanode in quantum dot sensitized solar cells for higher open circuit voltage, Chem. Phys. Lett. **761**, 138099 (2020).
DOI: https://doi.org/10.1016/j.cplett.2020.138099

[38] P. Bai, S. Zheng, C. Chen, Electrochemical characteristics of the early corrosion stages of API X52 steel exposed to H2S environments, Mater. Chem. Phys. **149-150**, (2015).
DOI: http://dx.doi.org/10.1016/j.matchemphys.2014.10.020

[39] M. Javidi, S. Bahalaou Horeh, Investigating the mechanism of stress corrosion cracking in near-neutral and high pH environments for API 5L X52 steel, Corros. Sci. **80**, 213 (2014).
DOI: https://doi.org/10.1016/j.corsci.2013.11.031

[40] A.Q. Fu, X. Tang, Y.F. Cheng, Characterization of corrosion of X70 pipeline steel in thin electrolyte layer under disbonded coating by scanning Kelvin probe, Corros. Sci. **51**, 186 (2009).
DOI: https://doi.org/10.1016/j.corsci.2008.10.018

[41] F.F. Eliyan, E.S. Mahdi, A. Alfantazi, Electrochemical evaluation of the corrosion behavior of API-X100 pipeline steel in aerated bicarbonate solutions, Corros. Sci. **58**, 181 (2012).
DOI: https://doi.org/10.1016/j.corsci.2012.01.015

[42] F. Xie, X. Li, D. Wang, M. Wu, D. Sun, Synergistic effect of sulphate-reducing bacteria and external tensile stress on the corrosion behaviour of X80 pipeline steel in neutral soil environment, Eng. Fail. Anal. **91**, 382 (2018).
DOI: https://doi.org/10.1016/j.engfailanal.2018.03.023

[43] M. Alizadeh, S. Bordbar, The influence of microstructure on the protective properties of the corrosion product layer generated on the welded API X70 steel in chloride solution, Corros. Sci. **70**, (2013).
DOI: https://doi.org/http://dx.doi.org/10.1016/j.corsci.2013.01.026

[44] W. Zhao, Y. Zou, D.X. Xia, Z.D. Zou, Effects of anodic protection on SCC behavior of X80 pipeline steel in high-pH carbonate-bicarbonate solution, Arch. Metall. Mater. **60**, 1009 (2015).
DOI: https://doi.org/10.1515/amm-2015-0251

[45] R.N. Parkins, S. Zhou. The stress corrosion cracking of C-Mn steel in CO_2-HCO_3^--CO_3^{2-} solutions. II: electrochemical and other data, Corros. Sci. **39**, (1997).

[46] A. Torresislas, V. Salinasbravo, J. Albarran, J. Gonzalezrodriguez, Effect of hydrogen on the mechanical properties of X-70 pipeline steel in diluted solutions at different heat treatments, Int. J. Hydrogen. Energ. **30**, 1317 (2005).
DOI: https://doi.org/10.1016/j.ijhydene.2005.04.007

[47] J.S. Elzbieta Sikora, Digby D. Macdonald, A new method for estimating the diffusivities of vacancies in passive films, Electrochim. Acta. **41**, (1996).

[48] X. Du, X. Dai, Z. Li, X. Du, H. Shi, J. Wu, H. Lou, X. Feng, L. Zhao, Z. Li, Corrosion analysis and anti-corrosion measures of oil casing of sulfur content gas wells: A case study of Daniudi gas field in the Ordos Basin, Energy Rep. **7**, 1280 (2021).
DOI: https://doi.org/10.1016/j.egyr.2021.02.041

[49] A. Fragiel, S. Serna, R. Pérez, Electrochemical study of two microalloyed pipeline steels in H2S environments, Int. J. Hydrogen. Energ. **30**, (2005).
DOI: http://dx.doi.org/10.1016/j.ijhydene.2005.04.006

[50] Y.D. Han, H.Y. Jing, L.Y. Xu, Welding heat input effect on the hydrogen permeation in the X80 steel welded joints, MaterChemPhys. **132**, 216 (2012).
DOI: https://doi.org/10.1016/j.matchemphys.2011.11.036

[51] P. Bai, S. Zheng, H. Zhao, Y. Ding, J. Wu, C. Chen, Investigations of the diverse corrosion products on steel in a hydrogen sulfide environment, Corros. Sci. **87**, (2014).
DOI: http://dx.doi.org/10.1016/j.corsci.2014.06.048

[52] C. Zhou, X. Chen, Z. Wang, S. Zheng, X. Li, L. Zhang, Effects of environmental conditions on hydrogen permeation of X52 pipeline steel exposed to high H2S-containing solutions, Corros. Sci. **89**, (2014). DOI: http://dx.doi.org/10.1016/j.corsci.2014.07.061

[53] W. Zhao, Y. Zou, K. Matsuda, Z. Zou, Corrosion behavior of reheated CGHAZ of X80 pipeline steel in H2S-containing environments, Mater. Design. **99**, 44 (2016).

[54] Neetu, P.K. Katiyar, S. Sangal, K. Mondal, Effect of various phase fraction of bainite, intercritical ferrite, retained austenite and pearlite on the corrosion behavior of multiphase steels, Corros. Sci. **178**, 109043 (2021).
DOI: https://doi.org/10.1016/j.corsci.2020.109043

[55] L. Gan, F. Huang, X. Zhao, J. Liu, Y.F. Cheng, Hydrogen trapping and hydrogen induced cracking of welded X100 pipeline steel in H_2S environments, Int. J. Hydrogen. Energ. **43**, (2018).

[56] A.A. Saleh, D. Hejazi, A.A. Gazder, D.P. Dunne, E.V. Pereloma, Investigation of the effect of electrolytic hydrogen charging of X70 steel: II. Microstructural and crystallographic analyses of the formation of hydrogen induced cracks and blisters, Int. J. Hydrogen. Energ. **41**, 12424 (2016).
DOI: https://doi.org/10.1016/j.ijhydene.2016.05.235

[57] H. Tian, J. Xin, Y. Li, X. Wang, Z. Cui, Combined effect of cathodic potential and sulfur species on calcareous deposition, hydrogen permeation, and hydrogen embrittlement of a low carbon bainite steel in artificial seawater, Corros. Sci. **158**, 108089 (2019).
DOI: https://doi.org/10.1016/j.corsci.2019.07.013

[58] O. Lavigne, E. Gamboa, V. Luzin, M. Law, Analysis of intergranular stress corrosion crack paths in gas pipeline steels; straight or inclined?, Eng. Failure Anal. **85**, (2018).